



- 1 Variations of the 630.0 nm airglow emission with meridional
- 2 neutral wind and neutral temperature around midnight
- 3 Chih-Yu Chiang¹, Sunny Wing-Yee Tam¹, Tzu-Fang Chang^{1,2}
- 4 ¹ Institute of Space and Plasma Sciences, National Cheng Kung University, Tainan
- 5 70101, Taiwan
- 6 ² Institute for Space-Earth Environmental Research, Nagoya University, Nagoya
- 7 464-8601, Japan



8 **Abstract**

9 Enhancements in 630.0 nm airglow around midnight at equatorial latitudes were
10 observed by many optical observations. Such features had been suggested as the
11 signature of thermospheric midnight temperature maximum (MTM) effect, which was
12 associated with temperature and meridional neutral winds. This study investigates the
13 influence of neutral temperature and meridional neutral wind on the volume emission
14 rates of the 630.0 nm nightglow. We utilize the SAMI2 model to simulate the charged
15 and neutral species at the 630.0 nm nightglow emission layer under different
16 temperatures with and without the effect of neutral wind. The results show that the
17 neutral wind is more efficient than temperature variation in affecting the nightglow
18 emission rates. However, the emission rate features a local maximum in its variation
19 with the temperature. Two kinds of tendencies can be seen regarding the temperature
20 that corresponds to the turning point, which is named the turning temperature (T_t) in
21 this study: firstly, T_t decreases with the emission rate for the same altitude; secondly,
22 for approximately the same emission rate, T_t increases with the altitude.

23

24

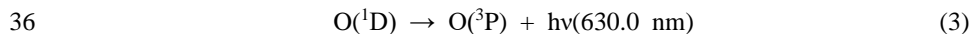
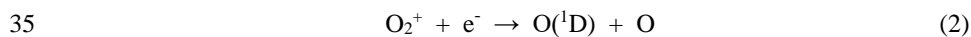
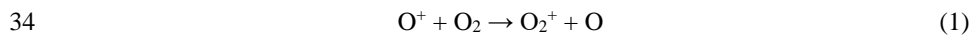
25

26



27 **1. Introduction**

28 The atomic oxygen red line at 630.0 nm is the most prominent emission in the
29 nighttime ionosphere. It usually forms an emission layer in the F region at altitudes of
30 ~200–300 km and can be easily observed from ground-based observatories or
31 satellites [Nelson and Cogger, 1971; Kelley et al., 2002; Thuillier et al., 2002]. The
32 emission is related to O(¹D), whose production in the nighttime is mainly via the
33 charge exchange and dissociative chemical processes listed as follows:



37 Based on the $[\text{O}^+] \sim N_e$ (electron density) approximation [Peterson et al., 1966;
38 Link and Cogger, 1988] in the F2 region, the intensity of the OI(¹D) 630.0 nm spectral
39 line is usually used to identify the ionospheric electron density variations. From a rich
40 history in the literature, the intensity of OI(¹D) 630.0 nm airglow emissions is
41 known as Midnight Brightness Wave (MBW) [Herrero and Meriwether, 1980;
42 Herrero et al., 1993; Colerico et al., 1996; Colerico and Mendillo, 2002].

43 During occurrences of MBW, enhancements in temperature are usually
44 observed around local midnight, which are termed Midnight Temperature Maximum
45 (MTM) effect. Harper [1973] and Spencer et al. [1979] first reported the MTM



46 phenomenon. The cases in their studies were observed by the incoherent scatter radar
47 from Arecibo and the NATE experiment aboard the Atmospheric Explorer E (AE-E)
48 satellite, respectively. The amplitude of the temperature bulge was found to range
49 from 20 to 200 K [Spencer *et al.*, 1979; Burnside *et al.*, 1981; Colerico and Mendillo,
50 2002; Meriwether *et al.*, 2008]. In addition, a number of studies about midnight
51 brightness have reported the relation between *in-situ* temperature and neutral wind
52 measurements [e.g., Herrero and Meriwether, 1980; Sastri *et al.*, 1994, Colerico *et al.*,
53 1996, 2002; Otsuka *et al.*, 2003; Mukherjee *et al.*, 2006]. Adachi *et al.* [2010] showed
54 a 14-day time span of airglow observations obtained from the Asian sector by the
55 Imager of Sprites and Upper Atmospheric Lightning (ISUAL) [Chang *et al.*, 2012;
56 Chiang *et al.*, 2013] on board the FORMOSAT-2 satellite. On the basis of the
57 observation time and location, they suggested that the equatorial airglow probably
58 corresponded to the midnight brightening wave (MBW) which is in association with
59 the occurrence of MTM. Furthermore, Chiang *et al.* [2013] statistically investigated
60 the global midnight brightness according to seasons and found that the global
61 midnight brightness near the equatorial regions was controlled by different
62 mechanisms. In the study, the features and behavior of the 630.0 nm midnight
63 intensity were investigated by analyzing the optical images obtained by ISUAL
64 (Supplement I). Cases of global midnight brightness were successfully categorized



65 into four types that were mainly due to the influence of temperature changes, neutral
66 wind and ionospheric anomaly.

67 Based on the previous studies, it is known that temperature and meridional
68 neutral wind are correlated and associated with manifestations of MTM. Thus, we
69 want to discuss these two effects at the same time. In this study, we calculate the volume
70 emission rates to understand the influence of neutral temperature and meridional
71 neutral wind on the 630.0 nm nightglow. We shall discuss the sensitivities of the
72 emission rates to the temperature and the densities of several neutral and charged
73 species. Moreover, some new features will also be shown in the discussion section.

74

75 2. Model features

76 Temperature changes and meridional neutral wind can influence the O(¹D)
77 nightglow intensity through particle densities. The volume emission rate of the 630.0
78 nm nightglow in the F2 region [Sobral *et al.*, 1993] can be derived from the
79 chemical process of 630.0 nm nightglow (Supplement II). It is shown as follows:

$$83 \quad I_{630} = \frac{A_{1D}\mu_D\gamma[O_2][O^+]}{k_1[N_2] + k_2[O_2] + k_3[O] + A_{1D} + A_{2D}}, \quad (4)$$

80 where μ_D is the quantum yield of O(¹D), which is about 1~1.3 [Torr and Torr, 1982]; γ
81 is the rate coefficient of Reaction (1) [St.-Maurice and Torr, 1978]; k_1 , k_2 and k_3 are
82 the rate coefficients of O(¹D) quenched by N₂, O₂ and O, respectively [Langford *et al.*,



84 1986; *Streit et al.*, 1976; *Sun and Dalgarno*, 1992]; and A_{1D} and A_{2D} are the transition
85 coefficients [*Froese-Fischer and Saha*, 1983]. The formulas for the rate coefficients
86 [*Vlasov et al.*, 2005] are listed in Table 1. The production rate of $O(^1D)$ is contributed
87 by the oxygen ion density $[O^+]$ and the molecular oxygen density $[O_2]$ through the
88 linked reactions (1) and (2). The major loss rates of $O(^1D)$ are associated with the
89 densities of molecular oxygen $[O_2]$, molecular nitrogen $[N_2]$, and atomic oxygen $[O]$,
90 as reflected in Eq. (4). The densities $[O^+]$, $[O_2]$, $[N_2]$ and $[O]$ and the rate coefficients
91 γ , k_1 , k_2 and k_3 all depend on temperature. In addition, $[O^+]$ may change with the
92 neutral wind conditions. In order to determine I_{630} under different temperatures and
93 neutral wind conditions, one must first determine the densities of the relevant species.
94 In this study, $[O^+]$ and plasma temperatures under various conditions are found by the
95 SAMI2 model of the Naval Research Lab [*Huba et al.*, 2000]. SAMI2 is a two-
96 dimensional, first-principle model of the comprehensive low to mid-latitude
97 ionosphere. SAMI2 code includes most of the mechanisms that should be considered
98 in the ionosphere. There are photoionizations, chemical process, effects by the
99 magnetic and electric fields, plasma dynamics and the influence from the neutral
100 atmosphere. The input variables, neutral species, are specified using the empirical
101 codes, the Mass Spectrometer Incoherent Scatter model (NRLMSISE-00) [*Picone et*
102 *al.*, 2002] for neutral densities and the Horizontal Wind Model (HWM-93) [*Hedin et*



103 *al.*, 1996] for neutral wind. The continuity and momentum equations of seven ion
104 species (H^+ , He^+ , N^+ , O^+ , N_2^+ , NO^+ , and O_2^+) are solved in the code.

105 In order to understand the differences due to the meridional neutral wind, we
106 apply the SAMI2 model with and without neutral wind by changing the multiplicative
107 factor of neutral wind ($tvn0$) to see the differences between two solstices. Thus, we
108 simulate the cases of February 1, 2007 (northern winter) and August 1, 2007 (northern
109 summer). In the simulations, we suppose that the solar and geomagnetic activities are
110 in quiet conditions ($F10.7$ index = 60, A_p index = 7). The simulations are run for the
111 altitude range between 150 and 1000 km from -30° to $+30^\circ$ geomagnetic latitudes.
112 Inside this region, we use 100 geomagnetic field lines and 201 grid points along the
113 field line. Our report of the results will focus on the locations at -5° and $+5^\circ$
114 geomagnetic latitude ($+2^\circ$ and $+12^\circ$ geographic latitude respectively) along the $100^\circ E$
115 geographic longitude, which intersects these latitudes in the Asian region. Figure 1
116 shows the O^+ density along the magnetic lines with apex altitudes between 265 and
117 315 km in the latitude-altitude plane at the time and longitude described above. Figure
118 1(a) shows the results under the condition that lacks neutral wind, and Fig. 1(b) shows
119 the results with the effect of normal neutral wind. The two left panels are for February
120 1, 2007 and the two right panels are for August 1, 2007. The arrows plotted in Fig. 1(b)
121 indicate the strength and directions of the meridional neutral wind. Comparison of Fig.



122 1(a) and 1(b) clearly shows that meridional winds transport the plasma along the
123 magnetic field line and change the plasma density distribution. And this change of the
124 plasma profile could directly modify the emission rate in Eq. (4). The dashed lines,
125 which correspond to $\pm 5^\circ$ geomagnetic latitude, indicate the locations where the
126 intensity of the 630.0 nm nightglow is examined in detail in this study.

127

128 **3. Results and Analysis**

129 Based on Eq. (4), I_{630} under different temperatures and different neutral wind
130 conditions is plotted in Fig. 2. The neutral wind conditions for the results in Fig. 2 are
131 the same as those for Fig. 1. The strength and directions of the neutral winds are
132 indicated by the arrows shown in Fig. 1. The simulation results shown in the figure
133 are for (a) February 1, 2007 and (b) August 1, 2007, with the left and right panels
134 respectively corresponding to -5° and $+5^\circ$ geomagnetic latitude. The letters, A, B, C,
135 D and E, indicate the altitudes of 220, 230, 240, 250 and 260 km, respectively. The
136 dotted lines indicate the results with normal neutral wind effect; the solid lines
137 indicate the results without neutral wind effect. Note that the temperatures of around
138 650°K, corresponding to the leftmost points of the lines in the figure, were the initial
139 neutral temperatures obtained from the NRLMSISE-00 model at the various altitudes.
140 These neutral temperatures are input into the SAMI2 model, and we set up the



141 48-hour data as a running loop to obtain the plasma data. For different temperature
142 conditions, we increase 50 K in the input temperature every time via modifying the
143 codes of SAMI2 and ran the simulations to calculate new values for the emission
144 intensity.

145 From Fig. 2, we can see the influence of temperature and neutral wind on the
146 nightglow emission. Note that the neutral wind conditions are as in Fig. 1: Fig. 1(a)
147 for without wind condition and the Fig. 1(b) for normal wind condition. The influence
148 of the temperature variations on I_{630} is usually less than 3 photons/cm³/sec at the
149 heights of 220 to 260 km. The variation of I_{630} with temperature, however, is not
150 monotonic; there is a maximum in the intensity as the temperature changes. In terms
151 of height, as I_{630} depends on the local neutral and charged particle densities in
152 accordance with Eq. (4), the emission is the strongest at 230 km, except for the
153 condition of very weak emission (< 1 photon/cm³/sec) that occurs at +5° geomagnetic
154 latitude in August with normal wind effect (right panel of Fig. 2(b)).

155 As for the influence of the neutral wind on February 1, 2007 of Fig. 2(a), both
156 locations ($\pm 5^\circ$ geomagnetic latitude) clearly feature significantly smaller I_{630} under
157 this effect. We suggest that this is due to the meridional neutral wind blowing
158 equatorward in both hemispheres (see Fig. 1) and pushing the plasma upward along
159 the field lines, reducing the local charged particle densities and consequently the



160 emission rates as well. On August 1, 2007 of Fig. 2(b), the neutral wind causes the
161 intensity at $+5^\circ$ geomagnetic latitude to decrease significantly for the same reason as
162 the wind direction is locally southward (equatorward). This equatorward neutral wind,
163 however, has an opposite effect on the intensity at -5° geomagnetic latitude; being
164 locally poleward, the wind pushes the plasma downward along the field lines,
165 increasing the local charged particle densities and consequently the emission rates as
166 well.

167 From Eq. (4), we can see that I_{630} is related to the densities of several neutral
168 species as well. In order to find out how the temperature affects the overall chemical
169 process that leads to the 630.0 nm emission, a few profiles of relevant parameters as
170 functions of temperature in Fig. 3, based on the condition at 230 km altitude and -5°
171 geomagnetic latitude on February 1, 2007. In Fig. 3(a), the $O(^1D)$ loss-rate terms
172 associated with $[O]$, $[N_2]$ and $[O_2]$, which are shown in dotted, dashed and solid lines
173 respectively. The value of $\gamma [O^+][O_2]$, which is related to the $O(^1D)$ production rate
174 and is in the numerator of Eq. (4), corresponding to Fig. 3(b). The dotted line
175 represents the normal neutral wind condition, and the solid line for the windless
176 condition.

177

178 **4. Discussion**



179 From Fig. 1(a), we can see that along the field lines, the O^+ density is maximum
180 around the geomagnetic equator when there is no neutral wind, whether it is in the
181 summer or winter season. But the $[O^+]$ maxima tilt to the winter hemisphere in the
182 presence of summer-to-winter neutral wind at the geomagnetic equator, as shown in
183 Fig. 1(b). The density profiles of the charged particles along the field lines are clearly
184 influenced by the neutral wind.

185 From the results that include the normal wind effect as shown in Fig. 2, the
186 intensities on opposite sides of the geomagnetic equator are very different. The
187 weaker emission is in the summer hemisphere, and brightness of higher intensity
188 appears in the winter hemisphere. In previous studies, *Rishbeth and Setty* [1961]
189 found that NmF2 was larger in winter than in summer, and they first suggested the
190 possibility of composition change being the cause of the winter anomaly. *Rishbeth*
191 [1972] and *Torr and Torr* [1973] suggested that the anomaly might be due to
192 transequatorial neutral wind blowing from the summer hemisphere to the winter
193 hemisphere. Therefore, the enhancement of the emission at the low latitudes of the
194 winter hemisphere should be the results of plasma accumulation caused by the neutral
195 wind effect.

196 Figure 2 shows the influence of temperature and neutral wind on the nightglow
197 emission rates. We estimate the intensity change under different neutral wind



198 conditions based on the location at 230 km altitude and -5° geomagnetic latitude on
199 February 1, 2007. In this situation, the emission would be reduced by the wind flow,
200 and the average change is about $0.690 \text{ photon/cm}^3/\text{sec}$ for every m/sec of the wind
201 speed. In comparison, the change due to temperature variation is just 0.015
202 $\text{photon/cm}^3/\text{sec}$ for every K. The ratio of the two numbers is 46. Consideration of
203 other conditions may reduce the corresponding ratio, but it should still be at least 20.
204 According to earlier studies, the neutral wind speed is generally 0-300 m/sec in the F
205 region [Dyson *et al.*, 1997], while the amplitude of the temperature bulge due to the
206 MTM effect has been found to range from 20 to 200 K [Burnside *et al.*, 1981;
207 Colerico and Mendillo, 2002]. Even if one assumes the maximum wind speed is just
208 60 m/sec as in the simulations in this study, it would require a temperature change of
209 1200 K to match the same change in emission intensity caused by the neutral wind.
210 Such a large temperature change is not realistic in comparison with the maximum
211 observed difference of 200 K. Thus, the emission rate of nightglow, realistically, is
212 influenced more by the neutral wind than temperature change when the former
213 mechanism is clearly present.

214 Previously Chiang *et al.* [2013] examined the occurrence rates of global midnight
215 brightness observed by FORMOSAT-2/ISUAL. In order to verify the enhancement of
216 the emission intensity in the winter hemisphere by the neutral wind, we examined the



217 FORMOSAT-2/ISUAL data that correspond to the specific regions and seasons
218 considered in our simulations and the results are shown in Fig. 4(a) and (b). We found
219 that among the 22 valid observation days during January and February, ~77% of the
220 days featured the appearance of nightglow bright spots in the low-latitude region of
221 the winter hemisphere (Fig. 4(a)). Furthermore, ~83% of the 30 valid observation
222 days during July-August also featured nightglow bright spots at low latitudes in the
223 corresponding winter hemisphere (Fig.4(b)). Thus, statistical results regarding the
224 location of nightglow bright spots agree with the simulation results that demonstrate
225 the crucial role of the neutral wind in affecting the location of high-intensity
226 nightglow regions.

227 The densities and some of the rate coefficients are temperature dependent, as
228 given in Eq. (4). We analyze the change with temperature of the individual terms in
229 Eq. (4) change with temperature. In Fig. 3(a) and Fig. 3(b), we shown the terms in the
230 numerator and denominator on the right-hand side of Eq. (4) and found that all these
231 terms increase with temperature. However, if we consider the derivative of the terms
232 with respect to temperature, which characterizes how sensitive the terms are to
233 temperature change, we notice that the derivatives for $k_1[\text{N}_2]$ and $k_3[\text{O}]$ increase with
234 temperature while those for $k_2[\text{O}_2]$ and $\gamma [\text{O}^+][\text{O}_2]$ decrease, as shown in Fig. 3(a)
235 and 3(b). How the variations of these terms affect the dependence of I_{630} on



236 temperature can now be understood from the right-hand side of Eq. (4). In particular,
237 the numerator, which characterizes the production rate of $O(^1D)$ and is proportional to
238 $\gamma [O^+][O_2]$, increases with temperature while featuring a relatively large increase at
239 lower temperatures (less than ~ 750 K). On the other hand, the denominator, which
240 characterizes the total loss rate of $O(^1D)$ and is dominated by $k_I[N_2]$ as Fig. 3(a)
241 indicates, features a relatively large increase at higher temperatures (larger than ~ 750
242 K). Upon division of the numerator by the denominator, the plot of I_{630} vs.
243 temperature is thus characterized by quasi-parabolic lines with the presence of a local
244 maximum --- or a turning point in the curve --- as shown in Fig. 2. We refer to the
245 temperature that corresponds to such a local maximum as the turning temperature (T_t).
246 Below T_t , I_{630} increases with temperature, meaning that the increase in the production
247 of $O(^1D)$ associated with a rise in the temperature is more efficient than the increase in
248 its loss. In contrast, I_{630} decreases with temperature above T_t , meaning that the
249 increase in the production of $O(^1D)$ associated with a rise in the temperature is less
250 efficient than the increase in its loss. Thus, T_t has the significance of being the
251 temperature at which the production and loss rates of $O(^1D)$ are equally sensitive to a
252 temperature change.

253 Figure 5 shows a plot of T_t versus the emission rate I_{630} at specific altitudes. The
254 results include all the cases shown in Fig. 2 with different symbols indicating different



255 altitudes. Two kinds of tendencies can be seen from the plot: firstly, T_t decreases with
256 I_{630} for the same altitude; secondly, for approximately the same emission rate, T_t
257 increases with the altitude. This is the first result to show these tendencies of the
258 turning temperature.

259 Observations of the movement of MTM temperature bulge and that of nightglow
260 have led to postulations of an association between pressure bulge and nightglow
261 intensity [Colerico *et al.*, 1996; Colerico and Mendillo, 2002; Meriwether *et al.*,
262 2008]. However, the high intensities of the observed nightglow have not been
263 successfully reproduced using existing models incorporating the MTM effect, such as
264 the NCAR thermosphere-ionosphere-electrodynamic general circulation model
265 (TIEGCM), as pointed out by Colerico and Mendillo [2002] and Meriwether *et al.*
266 [2008]. Note that temperature was not included as a varying quantity in traditional
267 ionospheric models. Thus the simulation study of temperature effect upon nightglow
268 intensity is lacking. Our simulation results have demonstrated the unexpectedly
269 non-monotonic dependence of the intensity of nightglow on the neutral temperature,
270 with the turning temperature T_t that arises from the dependence implying a limitation
271 for the growth of the emission rates. As the temperature increases above T_t , the
272 emission rates do not continue to grow. In fact, temperature change such as in the case
273 of heat transfer is affected by the density, which controls the heat capacity. At the



274 same time, temperature change may generate pressure difference and lead to transport
275 that changes density profiles. As nightglow intensity depends also on particle densities,
276 its non-monotonic variations with temperature are in fact due to the combination of
277 temperature and density. While our study suggests that neutral wind is the dominant
278 drive of the I_{630} variation, its influence, however, is via transportation of plasma and
279 neutral particles, in which case consideration of the effect of temperature on the
280 density is essential. Moreover, it has not been established that MTM is affected by the
281 wind primarily. The combination of temperature and density, which has shown to
282 cause non-monotonic results in this study, may very well be an important factor in the
283 study of MTM. Thus, if one wants to fully reproduce the observation results, we
284 suggest other extra factors associated with temperature variations should also be
285 considered, such as different tidal modes from lower atmosphere [Akmaev *et al.*,
286 2009]. Our findings of the turning temperature tendencies can help as a guide for
287 choosing the background temperature in future modeling attempts to obtain intensities
288 of nightglow brightness comparable to those observed from ground or from space.

289 Shepherd [2016] investigates the possible extent of the MTM at $\sim 20^\circ\text{N}$ – 40°N ,
290 considering O(1D) airglow volume emission rates, Doppler temperatures, and neutral
291 (zonal and meridional) observations by the Wind Imaging Interferometer (WINDII)
292 experiment on board the Upper Atmosphere Research Satellite (UARS). Their results



293 provide us the relations of the zonal wind to the $O(^1D)$ emission rate and of the
294 meridional wind to the temperature. Thus, it potentially leads us to a more extensive
295 future study in simulation to reproduce the observation and statistical results provided
296 by Shepherd in 2016.

297

298 **5. Conclusion**

299 Previous studies of the MTM effect have pointed out that the temperature
300 anomaly influences the nighttime behavior of the thermosphere. And the neutral wind
301 also plays a key role to cause the intensity variations in the nighttime ionosphere.
302 Based on our simulation results, both temperature change and meridional neutral wind
303 could cause the 630.0 nm nightglow intensity to vary while the latter is more effective.
304 An unexpected aspect of the results is the non-monotonic dependence of the emission
305 rate on temperature, featuring a turning point as the temperature changes. The
306 temperature T_t at which the turning point occurs corresponds to a balanced condition
307 between the production and loss of $O(^1D)$. Thus, our results help understand how the
308 overall chemical process of nightglow is affected by the variations of neutral
309 temperature and neutral wind. Two kinds of tendencies can be seen regarding the
310 turning temperature T_t . One is the higher T_t corresponding to higher altitude at the
311 same emission rate, the other is the higher T_t corresponding to lower emission rate at



312 the same altitude. Our findings of these turning temperature tendencies can guide

313 future modeling attempts to match the observed nightglow brightness intensities.

314

315 **Acknowledgements**

316 The authors acknowledge the FORMOSAT-2/ISUAL science and operator team

317 to provide image data (<http://sprite.phys.ncku.edu.tw/en/about-cdf-distribution>). The

318 work by C. Y. Chiang and S. W. Y. Tam is supported by Taiwan's Ministry of Science

319 and Technology grants MOST105-2111-M-006-007. T. F. Chang acknowledges

320 support by the Ministry of Education, Taiwan R.O.C., from The Aim for the Top

321 University Project to National Cheng Kung University.

322

323

324

325

326

327

328

329

330



331 **References**

- 332 Adachi, T., M. Yamaoka, M. Yamamoto, Y. Otsuka, H. Liu, C.-C. Hsiao, A. B. Chen,
333 and R.-R. Hsu (2010), Midnight latitude-altitude distribution of 630-nm airglow
334 in the Asian sector measured with FORMOSAT-2/ISUAL, *J. Geophys. Res.*,
335 doi:10.1029/2009JA015147.
- 336 Akmaev, R. A., F. Wu, T. J. Fuller-Rowell, and H. Wang (2009), Midnight
337 temperature maximum (MTM) in Whole Atmosphere Model (WAM)
338 simulations, *Geophys. Res. Lett.*, 36, L07108, doi:10.1029/2009GL037759.
- 339 Burnside, R. G., F. A. Herrero, J. W. Meriwether Jr., and J. C. G. Walker (1981),
340 Optical observations of thermospheric dynamics at Arecibo, *J. Geophys. Res.*,
341 86, 5532.
- 342 Chang, T. F., C. Z. Cheng, C. Y. Chiang, and A. B. Chen (2012), Behavior of substorm
343 auroral arcs and Pi2 waves: Implication for the kinetic ballooning instability,
344 *Ann. Geophys.*, 30, 911–926, doi:10.5194/angeo-30-911-2012.
- 345 Chiang, C. Y., T. F. Chang, S. W.-Y. Tam, T. Y. Huang, A. B.-C. Chen, H. T. Su, and R.
346 R. Hsu (2013), Global observations of the 630-nm nightglow and patterns of
347 brightness measured by ISUAL. *Terr. Atmos. Ocean. Sci.*, 24, 283-293, doi:
348 10.3319/TAO.2012.12.13.01(SEC)
- 349 Colerico, M., M. Mendillo, D. Nottingham, J. Baumgardner, J. Meriwether, J. Mirick,



- 350 B. W. Reinisch, J. L. Scali, C. G. Fesen, and M. A. Biondi (1996), Coordinated
351 measurements of F region dynamic related to the thermospheric midnight
352 temperature maximum, *J. Geophys. Res.*, 101, 26,783–26,793.
- 353 Colerico, M. J., and M. Mendillo (2002), The current state of investigations regarding
354 the thermospheric midnight temperature maximum (MTM), *J. Atmos. Sol. Terr.*
355 *Phys.*, 64, 1361– 1369.
- 356 Dyson, P. L., T. P. Davies, M. L. Parkinson, A. J. Reeves, P. G. Richards, and C. E.
357 Fairchild (1997), Thermospheric neutral winds at southern mid-latitudes: A
358 comparison of optical and ionosonde hmF2 methods, *J. Geophys. Res.*,
359 102(A12), 27189–27196, doi:10.1029/ 97JA02138.
- 360 Froese-Fischer, C., and H. P. Saha (1983), Multiconfiguration Hartree-Fock results
361 with Breit-Pauli corrections for forbidden transitions in the 2p4 configuration,
362 *Phys. Rev. A*, 28, 3169– 3178.
- 363 Harper, R. M. (1973), Nighttime meridional neutral winds near 350 km at low to
364 mid-latitudes, *J. Atmos. Terr. Phys.*, 35, 2023– 2034.
- 365 Hedin, A.E., E.L. Fleming, A.H. Manson, F.J. Schmidlin, S.K. Avery, R.R. Clark, S.J.
366 Franke, G.J. Fraser, T. Tsuda, F. Vial, and R.A. Vincent (1996), Empirical wind
367 model for the upper, middle, and lower atmosphere, *J. Atmos. Terr. Phys.*, 58,
368 1421-1447.



- 369 Herrero, F. A., and J. W. Meriwether Jr. (1980), 6300 airglow meridional intensity
370 gradients, *J. Geophys. Res.*, 85, 4191.
- 371 Herrero, F. A., N. W. Spencer, and H. G. Mayr (1993), Thermosphere and F-region
372 plasma dynamics in the equatorial region, *Adv. Space Res.*, 13(1), 201–220.
- 373 Huba, J. D., G. Joyce, and J. A. Fedder (2000), Sami2 is another model of the
374 ionosphere (SAMI2): A new low-latitude ionosphere model, *J. Geophys. Res.*,
375 105, 23,035–23,053.
- 376 Kelley, M. C., J. J. Makela, B. M. Ledvina, and P. M. Kintner (2002), Observations of
377 equatorial spread F from Haleakala, Hawaii, *Geophys. Res. Lett.*, 29(20), 2003,
378 doi:10.1029/2002GL015509.
- 379 Langford, A. O., V. M. Bierbaum, and S. R. Leone (1986), Branching ratios for
380 electronically excited oxygen atoms formed in the reaction of N⁺ with O₂ at
381 300 K, *J. Chem. Phys.*, 84, 2158–2166.
- 382 Link, R., and L. L. Cogger (1988), A reexamination of the OI 6300 Å nightglow, *J.*
383 *Geophys. Res.*, 93(A9), 9883-9892.
- 384 Meriwether, J., Faivre, M., Fesen, C., Sherwood, P., and Veliz, O (2008), New results
385 on equatorial thermospheric winds and the midnight temperature maximum,
386 *Ann. Geophys.*, 26, 447–466.
- 387 Mukherjee, G. K., N. Parihar, K. Niranjana, and G. Manju (2006), Signature of



- 388 midnight temperature maximum (MTM) using OI 630 nm airglow, *Indian J.*
389 *Radio Space Phys.*, 35,14–21.
- 390 Nelson, G. J., and L. L. Cogger (1971), Dynamical behavior of the nighttime
391 ionosphere at Arecibo, *J. Atmos. Terr. Phys.*, 33, 1711 – 1726,
392 doi:10.1016/0021-9169(71)90219-4.
- 393 Otsuka, Y., T. Kadota, K. Shiokawa, T. Ogawa, S. Kawamura, S. Fukao, and S.-R.
394 Zhang (2003), Optical and radio measurements of a 630-nm airglow
395 enhancement over Japan on 9 September 1999, *J. Geophys. Res.*, 108(A6), 1252,
396 doi:10.1029/2002JA009594.
- 397 Peterson, V. L., T. E. Van Zandt, and R. B. Norton (1966), F-region nightglow
398 emissions of atomic oxygen, 1. Theory, *J. Geophys. Res.*, 71, 2255-2265.
- 399 Picone, J. M., A. E. Hedin, D. P. Drob, and A. C. Aikin (2002), NRLMSISE-00
400 empirical model of the atmosphere: Statistical comparisons and scientific issues,
401 *J. Geophys. Res.*, 107(A12), 1468, doi:10.1029/2002JA009430
- 402 Rishbeth, H., and C. S. G. K. Setty (1961), The F layer at sunrise, *J. Atmos. Terr.*
403 *Phys.*, 20, 263-267.
- 404 Rishbeth, H. (1972), Thermospheric winds and the F-region – A review, *J. Atmos. Terr.*
405 *Phys.*, 34, 1.
- 406 Sastri, J. H., H. N. R. Rao, V. V. Somayajulu, and H. Chandra, Thermospheric winds



- 407 associated with equatorial midnight temperature maximum (MTM), *Geophys.*
408 *Res. Lett.*, **21**, 825, 1994.
- 409 Shepherd, M. G. (2016), WINDII observations of thermospheric O(1D) nightglow
410 emission rates, temperature, and wind: 1. The northern hemisphere midnight
411 temperature maximum and the wave 4, *J. Geophys. Res. Space Physics*, 121,
412 doi:10.1002/2016JA022703.
- 413 Sobral, J. H.A., H. Takahashi, M. A. Abdu, P. Muralikrishna, Y. Sahai, C. J. Zamlutti,
414 E. R. de Paula, and P. P. Batista (1993), Determination of the quenching rate of
415 the O(¹D) by O(³D) from rocket-borne optical (630 nm) and electron density
416 data, *J. Geophys. Res.*, **98**, 7791-7798.
- 417 Spencer, N. W., C. R. Carignan, H. G. Mayr, H. B. Niemann, R. F. Theis, and L. E.
418 Wharton (1979), The midnight temperature maximum in the Earth's equatorial
419 thermosphere, *Geophys. Res. Lett.*, **6**, 444.
- 420 St. Maurice, J. P., D. G. Tort, Nonthermal rate coefficients in the ionosphere: The
421 reactions of O₂⁺ with N₂, O₂, and NO, *J. Geophys. Res.*, **83**, 969, 1978.
- 422 Streit, G. E., C. J. Howard, A. L. Schmeltekopf, J. J. A. Davidson, and H. I. Schiff
423 (1976), Temperature dependence of O(1D) rate constants for reactions with O₂,
424 N₂, CO₂, O₃ and H₂O, *J. Chem. Phys.*, **65**, 4761– 4764.
- 425 Sun, Y., and A. Dalgarno (1992), Collisional excitation of metastable O(1D) atoms, *J.*



426 Chem. Phys., 96, 5017– 5019.

427 Thuillier, G., R. H. Wiens, G. G. Shepherd, and R. G. Roble (2002), Photochemistry
428 and dynamics in thermospheric intertropical arcs measured by the WIND
429 Imaging Interferometer on board UARS: A comparison with TIE-GCM
430 simulations, *J. Atmos. Sol. Terr. Phys.*, 64, 405– 415,
431 doi:10.1016/S1364-6826(01)00109-2.

432 Torr, M. R. and D. G. Torr (1973), The seasonal behaviour of the F2-layer of the
433 ionosphere, *J. Atmos. Terr. Phys.*, 35, 2237.

434 Torr, M. R. and D. G. Torr (1982), The role of metastable species in the
435 thermosphere, *Rev. Geophys. and Space Phys.*, 20, 91–144.

436 Vlasov, M. N., M. J. Nicolls, M. C. Kelley, S. M. Smith, N. Aponte, and S. A.
437 Gonzalez (2005), Modeling of airglow and ionospheric parameters at Arecibo
438 during quiet and disturbed periods in October, 2002, *J. Geophys. Res.*, 110,
439 A07303, doi:10.1029/2005JA011074.

440

441

442

443

444



445 Table 1. Reactions and rate coefficients related to the volume emission rate of the
 446 630.0 nm airglow

Reactions	Rate Coefficients (cm ³ s ⁻¹ , s ⁻¹)
$O^+ + O_2 \rightarrow O_2^+ + O$	$\gamma = 2.82 \times 10^{-11} - 7.74 \times 10^{-12}(T_{\text{eff}}/300) + 1.07 \times 10^{-12}(T_{\text{eff}}/300)^2 - 5.17 \times 10^{-14}(T_{\text{eff}}/300)^3 + 9.65 \times 10^{-16}(T_{\text{eff}}/300)^4$
$O(^1D) + N_2 \rightarrow O + N_2$	$k_1 = 2 \times 10^{-11} \exp(107.8/T_n)$
$O(^1D) + O_2 \rightarrow O + O_2$	$k_2 = 2.9 \times 10^{-11} \exp(67.5/T_n)$
$O(^1D) + O \rightarrow O + O$	$k_3 = (3.73 + 1.1965 \times 10^{-1} T_n^{0.5} - 6.5898 \times 10^{-4} T_n) \times 10^{-12}$
$O(^1D) \rightarrow O + h\nu(630.0\text{nm})$	$A_{1D} = 7.1 \times 10^{-3}$
$O(^1D) \rightarrow O + h\nu(634.4\text{nm})$	$A_{2D} = 2.2 \times 10^{-3}$

447 Note: $T_{\text{eff}} = 0.67T_i + 0.33T_n$ (T_{eff} : effective temperature, T_i : ion temperature, T_n : neutral temperature)
 448 [*St.-Maurice and Torr, 1978*]

449

450

451

452

453

454

455

456

457

458

459

460

461



462 **Figure Captions**

463 Figure 1. Oxygen ion density plotted in the latitude-altitude plane at 23:00 LT on
464 February 1, 2007 (left panels) and August 1, 2007 (right panels) in the Asian
465 region (100°E longitude) from the SAMI-2 model: (a) without neutral wind; (b)
466 with the effect of normal neutral wind, whose strength and directions are
467 indicated by the arrows.

468 Figure 2. The results of 630.0 nm emission rate at 23 LT at different temperatures and
469 under different neutral wind conditions for (a) February 1, 2007 and (b) August
470 1, 2007: left and right panels respectively for -5° and +5° geomagnetic latitude;
471 the letters, A, B, C, D and E, for the altitudes of 220 km, 230 km, 240 km, 250
472 km and 260 km, respectively; for normal neutral wind effect (black dotted lines)
473 and windless conditions (red solid lines). The neutral wind conditions of Fig. 2
474 are the same as those shown in Fig. 1.

475 Figure 3. Profiles of the terms in Eq. (4) that are associated with neutral and charged
476 species versus temperature, based on 230 km altitude and -5° geomagnetic
477 latitude on February 1, 2007, with and without neutral wind: (a) the loss-rate
478 terms associated with [O], [N₂] and [O₂]; (b) the production-rate term γ
479 [O⁺][O₂].

480 Figure 4. FORMOSAT-2/ISUAL data in the specific regions and seasons considered



481 in our simulations: (a) Among the 22 valid observation days during
482 January-February, ~77% of the days featured the appearance of nightglow
483 bright spots in the low-latitude region of the winter hemisphere; (b) About 83%
484 of the 30 valid observation days during July-August also featured nightglow
485 bright spots at low latitudes in the corresponding winter hemisphere.

486 Figure 5. Plots of the emission rates against the turning temperature between 220-260
487 km altitudes.

488

489

490

491

492

493

494

495

496

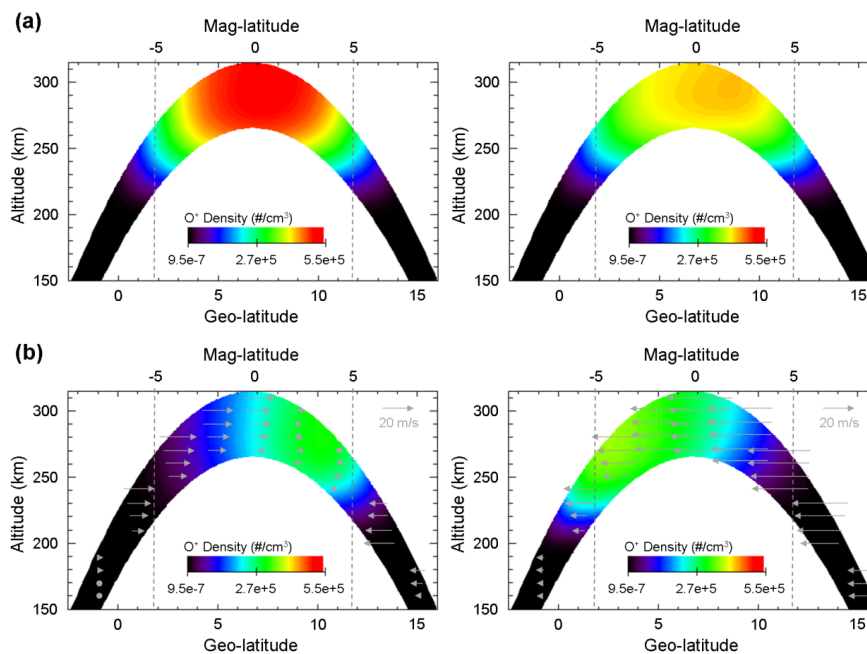
497

498

499



500 Figure 1



501

502

503

504

505

506

507

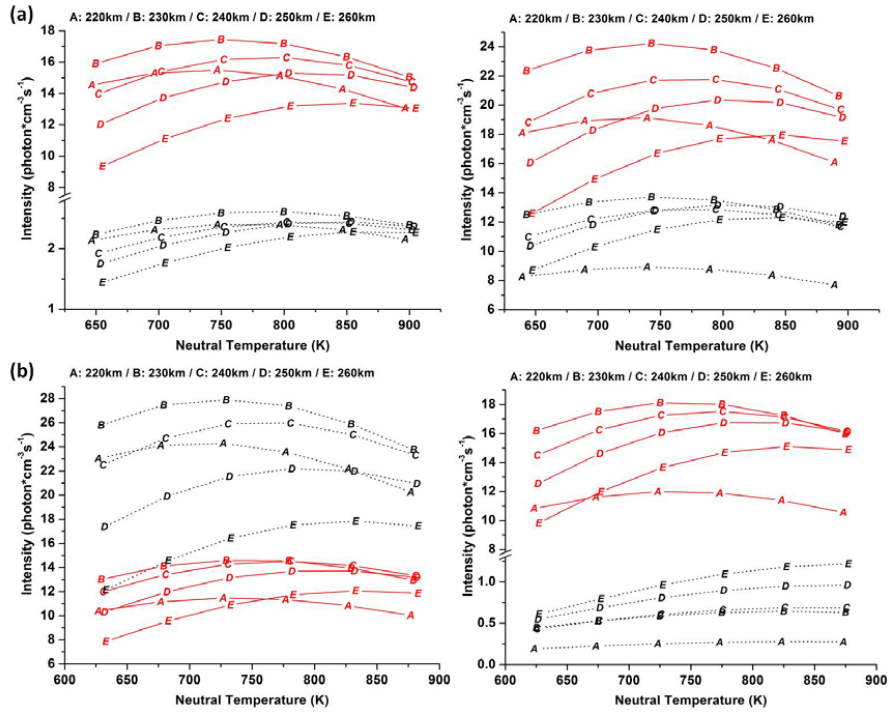
508

509

510



511 Figure 2



512

513

514

515

516

517

518

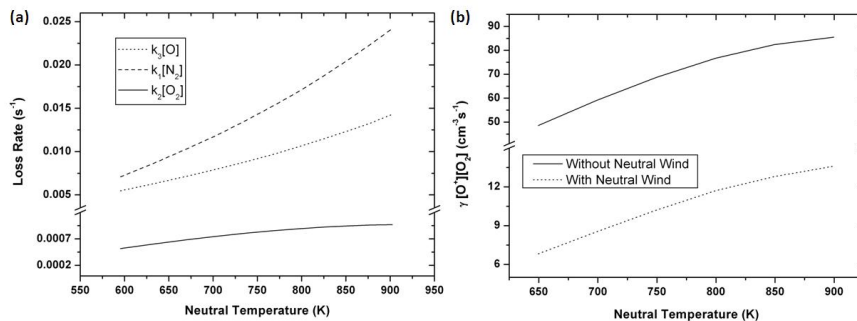
519

520

521



522 Figure 3



523

524

525

526

527

528

529

530

531

532

533

534

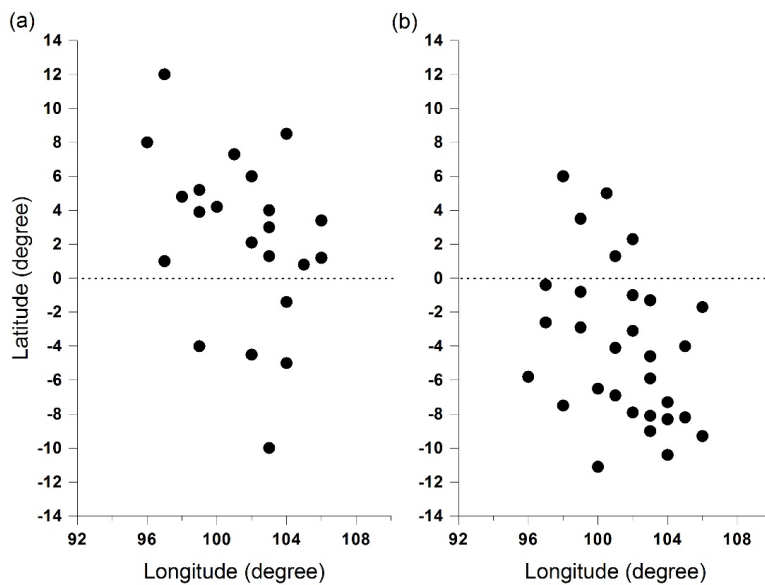
535

536

537



538 Figure 4



539

540

541

542

543

544

545

546

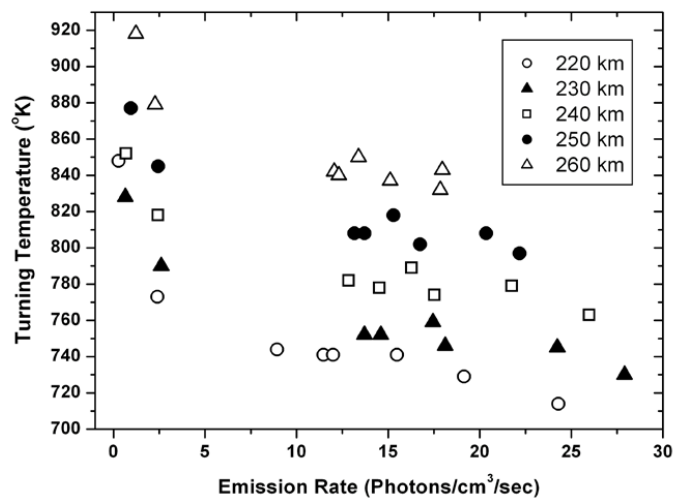
547

548

549



550 Figure 5



551